Chiral exciton wave functions in cylindrical *J* aggregates

Cătălin Didraga and Jasper Knoester[a)]
Institute for Theoretical Physics and Materials Science Center, University of Groningen, Nijenborgh 4, 9747 AG Groningen, The Netherlands

(Received 4 March 2004; accepted 22 April 2004)

We study the exciton wave functions and the optical properties of cylindrical molecular aggregates. The cylindrical symmetry allows for a decomposition of the exciton Hamiltonian into a set of effective one-dimensional Hamiltonians, characterized by a transverse wave number k_2. These effective Hamiltonians have interactions that are complex if the cylinder exhibits chirality. We propose analytical ansätze for the eigenfunctions of these one-dimensional problems that account for a finite cylinder length, and present a general study of their validity. A profound difference is found between the Hamiltonian for the transverse wave number $k_2=0$ and those with $k_2\neq 0$. The complex nature of the latter leads to chiral wave functions, which we characterize in detail. We apply our general formalism to the chlorosomes of green bacteria and compare the wave functions as well as linear optical spectra (absorption and dichroism) obtained through our ansätze with those obtained by numerical diagonalization as well as those obtained by imposing periodic boundary conditions in the cylinder's axis direction. It is found that our ansätze, in particular, capture the finite-length effect in the circular dichroism spectrum much better than the solution with periodic boundary conditions. Our ansätze also show that in finite-length cylinders seven superradiant states dominate the linear optical response. © *2004 American Institute of Physics.*
[DOI: 10.1063/1.1762874]

I. INTRODUCTION

Lately, an increased interest has emerged in the optical properties and exciton dynamics of molecular aggregates with a cylindrical geometry. In nature, such aggregates exist as light-harvesting systems in the chlorosomes of green photosynthetic bacteria.[1] These light-harvesting systems are self-assembled aggregates consisting of bacteriochlorophyll (BChl) molecules, arranged in a cylindrical way. They are responsible for the absorption of sunlight and the transport of its energy in the form of excitons to the photosynthetic reaction centers in the base plate of the chlorosomes. On the basis of various kinds of spectroscopies and molecular modeling, a detailed model for the organization of the BChl molecules in these aggregates has been proposed.[2–6] In this model, the molecules form helices that wrap around a cylinder with a diameter of ~5 nm (for *Chloroflexus aurantiacus*) or ~10 nm (for *Chlorobium tepidum*) and a length that may reach several hundreds of nanometers. In the traditional language of molecular aggregates, these systems should be referred to as *J* aggregates, as their absorption band is red-shifted relative to that of a single BChl molecule.

Interestingly, cylindrical *J* aggregates have recently also been prepared synthetically, through self assembly of polymethine cyanine dye molecules with amphiphilic side groups.[7,8] Polymethine cyanine molecules are the prototype class of molecules that form self-assembled *J* aggregates. Due to their strong transition dipoles, they are among the molecules with the strongest tendency to self assemble, with the largest absorption strength, and the largest exciton transfer interaction.[9] Their special optical properties are the reason for their abundant use as light sensitizers in classical color photography.[10] In fact, their strong absorption and energy transport properties also make them ideal candidates to prepare synthetic light-harvesting systems. In this context, the new cylindrical aggregates of amphiphilic cyanine molecules are of great interest, as they closely mimic the natural antenna systems of green bacteria. Optical techniques and cryogenic transmission electron microscopy are employed abundantly to unravel the molecular arrangement and the microscopic properties of the cylindrical cyanine aggregates.[11–15] It has also been established that these synthetic cylindrical aggregates exhibit a chiral (helical) structure. In fact, chirality is an interesting and important property of many currently investigated (quasi-)one-dimensional supramolecular structures.[16,17]

In a recent study,[18] we have calculated the linear absorption, linear dichroism (LD), and circular dichroism (CD) spectra of cylindrical molecular aggregates and shown that the helicity may give rise to a complicated and seemingly erratic behavior of the CD spectrum with varying cylinder length. In our calculations we took advantage of the cylindrical symmetry by reducing the problem of finding the exciton eigenstates of the cylinder to the problem of solving for the eigenstates of a set of independent effective one-dimensional exciton systems. For general cylinder lengths, these effective systems were diagonalized numerically. For long cylinders, we also found analytical expressions for the spectra, by imposing periodic boundary conditions (PBC) along the direction of the cylinder's axis. In this limit, studied previously by Somsen *et al.*,[19] the linear spectra are gov-

[a)]Author to whom correspondence should be addressed. Electronic mail: knoester@phys.rug.nl

erned by three superradiant states. Unfortunately, while it is of obvious interest to have analytical expressions for the exciton wave functions and spectra as a function of the cylinder length, the analytical solution with PBC is strictly valid only in the limit of infinite length. Of course, one may impose PBC on cylinders with a finite length, but it turns out that, while for the absorption and LD spectra this gives reasonable results, for the calculation of the CD spectrum a finite cylinder length is incompatible with imposing PBC. This is due to the helical term in the CD spectrum,[18] which involves the relative position vector of pairs of molecules along the axis direction. A similar type of size consistency problem occurs for the absorption spectrum in tight-binding models for one-dimensional electron systems, in which the dipole is given by the electron position measured along the direction in which one would like to apply PBC.[20,21] For the electron chains, this problem may be solved by making the chain's geometry consistent with the PBC, i.e., by turning it into a circle. The equivalent for our cylinder would be to consider a torus arrangement, which, however, for general sizes destroys the cylindrical symmetry and only would be a reasonable approximation again at very large cylinder lengths.

Motivated by the above, we investigate in this paper analytical ansätze for exciton wave functions that explicitly account for the finite length of the cylinder and that also incorporate the helical nature of the system. In general, the problem to be solved boils down to diagonalizing one-dimensional exciton Hamiltonians which contain long-range interactions (which at long distances behave like dipolar interactions) and which, due to the helicity, in general lack inversion symmetry. In analogy to previous work for a symmetric exciton chain with point–dipole interactions,[22] we show that it is possible to find good analytical approximations to the optically dominant exciton states. These solutions may be separated into two types, distinguished by their transverse wave number ($k_2=0$ and $k_2=\pm 1$, respectively) describing the Bloch state in the circumferential direction of the cylinder. In the $k_2=\pm 1$ states, the helical nature of the cylinder plays a prominent role, leading to a clear chiral behavior of the wave functions.

The outline of this paper is as follows: In Sec. II we present the model and the reduction to effective one-dimensional Hamiltonians. In particular, we present the effective Hamiltonians $H(k_2=0)$ and $H(k_2=\pm 1)$ which describe the two classes of exciton states that are optically active. In Sec. III we study the exciton eigenfunctions of $H(k_2=0)$, while in Sec. IV we investigate the eigenfunctions and their optical selection rules for $H(k_2=\pm 1)$. Section V is dedicated to the application of our general results for the exciton eigenstates to the special case of the chlorosomes of *Chloroflexus aurantiacus*. Finally, in Sec. VI, we present our conclusions.

II. MODEL AND REDUCTION TO ONE-DIMENSIONAL PROBLEMS

For the cylindrical aggregates, we consider the same model of as we did previously,[18] depicted schematically in Fig. 1. The model consists of a perpendicular stack of N_1 rings of radius R, each one containing N_2 equidistant molecules. Adjacent rings are separated by a distance H are rotated relative to each other over a helical angle γ. We will label the molecules by a two-dimensional vector $\mathbf{n}=(n_1,n_2)$, where $n_1=1,2,\ldots,N_1$ gives the position along the helices (i.e., the ring number) and $n_2=1,2,\ldots,N_2$ labels the helix (i.e., the position along the ring). Each molecule is modeled as a two-level chromophore, with transition frequency ω_0 and with a transition dipole $\boldsymbol{\mu}_\mathbf{n}$ that is equal in magnitude (μ) for all molecules. Each molecular dipole makes an angle β with respect to the cylinder axis, while its projection on a plane perpendicular to this axis makes an angle α with the local tangent to the ring. The reader is referred to Ref. 18 for comments concerning the general nature of this model.

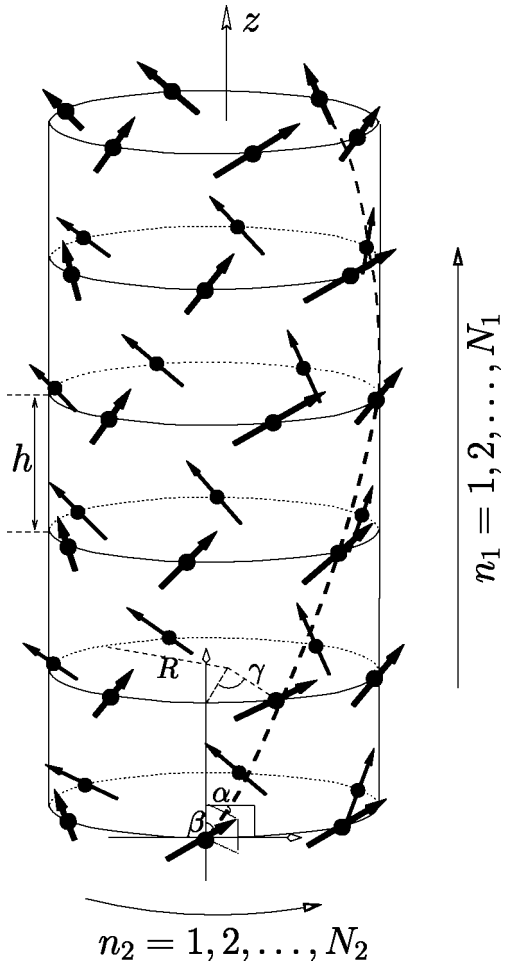

FIG. 1. Cylindrical aggregate consisting of a stack of N_1 rings, labeled $n_1=1,\ldots,N_1$, each containing N_2 molecules, labeled $n_2=1,\ldots,N_2$. The arrows indicate the molecular transition dipoles, which are all equal in magnitude (μ) and make an angle β with the cylinder axis. The projection of each dipole on the plane of the rings makes an angle α with the local tangent to the ring. Each ring is rotated with respect to the previous one over an angle γ, so that we may view the aggregate as a collection of N_2 parallel helices on the cylinder's surface. One such helix is indicated by the dashed curve.

The electronically excited states of the aggregate are described by a Frenkel exciton Hamiltonian on the above described two-dimensional manifold, with intermolecular excitation transfer interactions $J(\mathbf{m})=J(m_1,m_2)$ that are determined by the relative position vector $\mathbf{m}$ of the two molecules under consideration. This interaction is given by the

interaction between the transition dipoles of the two molecules. Using the cylindrical symmetry of the model, which prescribes a Bloch wave $\sim\exp(i2\pi k_2 n_2/N_2)$ $[k_2=0,\pm1, \pm2,\ldots,\pm(N_2/2-1),N_2/2]$[23] for the dependence of the exciton wave functions on n_2, the total Hamiltonian is easily decoupled into a set of N_2 effective one-dimensional Hamiltonians,[18] labeled by the transverse wave number k_2. This effective Hamiltonian reads:

$$H(k_2)=[\omega_0+J(0;k_2)]\sum_{n_1=1}^{N_1} c^{\dagger}_{n_1,k_2}c_{n_1,k_2} + \sum_{n_1,m_1=1}^{N_1}{}' \; J(n_1-m_1;k_2)c^{\dagger}_{n_1,k_2}c_{m_1,k_2}, \tag{1}$$

where $c^{\dagger}_{n_1,k_2}$ and c_{n_1,k_2} are the operators for creation and annihilation of an excitation of transverse wave number k_2 on the ring n_1, respectively, and the prime on the second summation excludes the term with $n_1=m_1$. Furthermore, $J(n_1-m_1;k_2)$ is the effective interaction for transfer of an exciton of wave number k_2 from ring m_1 to ring n_1. This effective transfer interaction is given by

$$J(m_1;k_2)=\sum_{m_2=1}^{N_2}{}' \; J(m_1,m_2)e^{-i2\pi k_2 m_2/N_2}, \tag{2}$$

where $J(m_1,m_2)$ is the intermolecular dipole–dipole interaction introduced above and the prime excludes the term with $m_2=0$ if $m_1=0$. In the effective one-dimensional model, each one of the rings plays the role of an effective site on a one-dimensional chain of length N_1, with effective transition frequency $\omega_0+J(0;k_2)$ [where the term $J(0;k_2)$ accounts for the dipole–dipole interactions between the molecules that reside in the same ring] and effective excitation transfer interactions given by $J(m_1;k_2)$ from site n_1 to site n_1+m_1.

The effective interactions $J(m_1;k_2)$ and $J(m_1;-k_2)$ are each other's complex conjugates, implying that $H(k_2)$ and $H(-k_2)$ have the same set of eigenvalues, while their corresponding eigenvectors are related by complex conjugation. This allows us to focus on $H(k_2)$ with $k_2\geqslant 0$, as all other eigenvalues and eigenvectors follow from those. It should also be stressed that the effective interaction $J(m_1;k_2)$ is complex in general, and as a result of the helicity $[J(m_1,m_2)\neq J(-m_1,m_2)]$, it lacks inversion symmetry: $J(m_1;k_2)\neq J(-m_1;k_2)$. Thus, the effective one-dimensional Hamiltonians also lack inversion symmetry; of course, they are Hermitian for all k_2. Only in the special case $k_2=0$, is the effective interaction real and the Hamiltonian has inversion symmetry.

We will be interested mainly in the bands with $k_2=0$ and $k_2=\pm1$, as these are the only ones that contribute to the linear optical spectra.[18] The general expressions for the linear absorption spectrum and the linear and circular dichroism spectra in terms of the eigenvalues and eigenfunctions of $H(k_2=0)$ and $H(k_2=\pm1)$ were given in Ref. 18 and will not be repeated here. As the band with $k_2=-1$ is related to the one with $k_2=1$ by complex conjugation (see above), we will concentrate in the remainder of this paper on two effective Hamiltonians: $H^0\equiv H(k_2=0)$ and $H^1\equiv H(k_2=1)$. To stress the one-dimensional nature of these Hamiltonians and to simplify the notation, we omit the index k_2 and label the effective sites simply as n (i.e., we drop the subscript "1"); the total length of the system is still denoted as N_1. The Hamiltonian of the $k_2=0$ and the $k_2=1$ bands then have matrix elements denoted by, respectively,

$$\langle n|H^0|m\rangle=(\omega_0+J^0(0))\delta_{n,m}+J^0(n-m)(1-\delta_{n,m}), \tag{3}$$

and

$$\langle n|H^1|m\rangle=(\omega_0+J^1(0))\delta_{n,m}+J^1(n-m)(1-\delta_{n,m}). \tag{4}$$

Here, $|n\rangle$ denotes the state of the linear chain in which site n is excited and all other sites are in the ground state. Furthermore, $J^0(m)=J(m;k_2=0)$ and $J^1(m)=J(m;k_2=1)$ denote the two relevant effective interactions. For future reference we note that the long-range behavior of both of these interactions is of the dipole–dipole type, i.e., for $|m|$ large ($|m|h\gg R$), both J^0 and J^1 drop off like $1/|m|^3$. The systematic long-range (multipole) expansions for $J^0(m)$ and $J^1(m)$ are given in Appendix A. The first correction to point–dipole interactions is on the order $1/|m|^5$ for $J^0(m)$ and $1/|m|^4$ for $J^1(m)$. At short distances, the effective interactions differ markedly from point–dipole ones, due to the finite radius R of the rings.

As we will see below, the band with $k_2=0$ and its Hamiltonian H^0 is fundamentally different from the $k_2=1$ band, with Hamiltonian H^1. As discussed above, H^0 is governed by real and symmetric interactions, while H^1 is essentially complex and not symmetric. This requires a different approach, which is why both cases are treated separately in Secs. III and IV, respectively. Moreover, we will find that the optical selection rules for the two bands differ. In particular, for predominantly negative intermolecular interactions (J aggregate), the optically allowed states for $k_2=0$ occur at the band bottom, while for $k_2=1$ they lie a finite energy above the band bottom.

III. EIGENSTATES OF H^0

The effective Hamiltonian H^0 describes a linear chain with real and symmetric interactions $J^0(m)$. In the long range ($|m|\gg 2R/h$), the interactions behave like point–dipole ones: $J(m)=-J/|m|^3$ with an effective nearest-neighbor interaction $-J=-2(N_2\mu^2/h^3)\cos^2\beta$ (see Appendix A), but at short distances the deviations from this limiting form in general are significant. The case of a chain with real and pure point–dipole interactions (i.e., $\sim 1/|m|^3$ for all values of m) was investigated before by Malyshev and Moreno,[22] by starting from a simple ansatz for the exciton wave functions. We will closely follow their strategy, being more careful, however, in defining the criterion for the validity of the ansatz. This care is of crucial importance for the $k_2=1$ case.

The ansatz which we make for the eigenstates of H^0 reads

$$|k\rangle=\sqrt{\frac{2}{N_1+1}}\sum_{n=1}^{N_1}\sin(k\phi n)|n\rangle, \tag{5}$$

with $\phi=\pi/(N_1+1)$ and $k=1,2,\ldots,N_1$. In the notation of Ref. 18 the state Eq. (5) takes the form of Eq. (47) in that reference, with k replacing k_1 and $\theta_{k_2=0}$ set to zero. The ansatz Eq. (5) is exact for a chain with nearest-neighbor interactions[24] and is based on the intuition that for large N_1 (small ϕ) and small wave number k, i.e., for eigenstates that slowly oscillate in space on the scale of the lattice constant, the long-range contributions to the interaction hardly affect the form of the eigenstate.[22] It should be noted that generally speaking the states with small values of k dominate the optical spectra,[25] implying that having a good approximation for the wave functions of these slowly varying states should give good approximations to the spectra. In particular, of the above states, the $k=1$ state contains 81% of the total oscillator strength in the limit of large N_1. For negative (positive) nearest-neighbor interactions, this state lies at the bottom (top) of the exciton band. We will assume that also for our long-range interactions $J^0(m)$ this property holds. For point–dipole interactions, numerical simulations confirm this.[25]

In Ref. 22 the validity of the ansatz Eq. (5) for the optically dominant states was argued by showing that the matrix elements of the actual Hamiltonian with dipolar interactions between states with different k values are small for $k\ll N_1$. It should be pointed out, however, that this is a necessary, but not sufficient condition for negligible mixing of different k states by the long-range interactions. The proper criterion for negligible mixing of states $|k\rangle$ and $|k'\rangle$ by the long-range interactions involves the mixing ratio

$$r_0(k,k')=\frac{|H^0_{k,k'}|}{|H^0_{k,k}-H^0_{k',k'}|}, \tag{6}$$

with $H^0_{k,k'}=\langle k|H^0|k'\rangle$. As for close values of k and k' the energy separation $|H_{k,k}-H_{k',k'}|$ decreases with increasing N_1, and the denominator in Eq. (6) plays an important role. In order to show that the ansatz Eq. (5) is a good one for the optically dominant states, we have to show that $r_0(k,k')\ll 1$ if either k or k' (or both) are among those states, i.e., in particular for one of them being 1.

Using the effective Hamiltonian Eq. (3) and the ansatz Eq. (5), we arrive at the following general expressions for the relevant matrix elements:

$$H^0_{k,k}=\omega_0+J^0(0)+2\sum_{m=1}^{N_1-1}J^0(m)\cos(k\phi m)+\frac{2}{N_1+1}\left[\cot(k\phi)\sum_{m=1}^{N_1-1}J^0(m)\sin(k\phi m)-\sum_{m=1}^{N_1-1}mJ^0(m)\cos(k\phi m)\right] \tag{7}$$

and for $k\neq k'$

$$H^0_{k,k'}=\frac{1+(-1)^{k-k'}}{2(N_1+1)}\left\{\cot\frac{(k+k')\phi}{2}\sum_{m=1}^{N_1-1}J^0(m)\times[\sin(k\phi m)+\sin(k'\phi m)]-\cot\frac{(k-k')\phi}{2}\times\sum_{m=1}^{N_1-1}J^0(m)[\sin(k\phi m)-\sin(k'\phi m)]\right\}. \tag{8}$$

In deriving these expressions, we used the symmetry of the interactions, $J^0(-m)=J^0(m)$. The fact that states with odd k are not coupled to those with even k reflects this symmetry. We also note that the third term in Eq. (7) is identical to the dispersion of a one-dimensional aggregate with PBC, with the exception that ϕ in the case of PBC is given by $2\pi/N_1$.[25] The fourth and fifth terms in Eq. (7) together are on the order of $1/N_1$ and give an explicit correction due to edge effects.

In order to estimate the mixing ratio $r_0(k,k')$, we have to estimate the summations in Eqs. (7) and (8), in particular for $N_1\gg 1$, which is the case of our interest as then we expect the ansatz Eq. (5) to be good. We will first do this for the case of a pure dipole–dipole interaction and in the end of this section consider corrections due to the deviations from $1/|m|^3$ behavior at short distances.

Thus, we start by assuming that the interactions for all m take the form $J^0(m)=-J/|m|^3$ (with $J^0(0)\equiv 0$) and estimate the mixing ratio $r_0(k,k')$. As argued above, we have to do this for one of the wave numbers (say k) referring to one of the optically dominant states (i.e., k on the order of unity), while for the other (k') we have to consider all other states. Clearly, however, $r_0(k,k')$ will be largest in the case of neighboring states, i.e., for $|k-k'|$ on the order of unity, as for long chains these states get close to degeneracy. We may thus limit ourselves to considering the situation where both k and k' are on order of unity. The only situation where this would not suffice, occurs if at certain high k values the unperturbed energy $\langle k|H^0|\ k\rangle$ happens to be equal to the one at small k values. We will assume that such degeneracy of the exciton band edge does not occur. We will check this assumption explicitly when applying the formalism in Sec. V.

For large N_1, the summations in Eqs. (7) and (8) may be written as

$$\sum_{m=1}^{N_1-1}m^\alpha J^0(m)F(m\phi)=\sum_{m=1}^{\infty}m^\alpha J^0(m)F(m\phi)-\int_{N_1}^{\infty}m^\alpha J^0(m)F(m\phi)dm, \tag{9}$$

with $\alpha=0$ or 1, and $F(m\phi)$ the appropriate combination of trigonometric functions of $m\phi$. Here, we have extended the summation to infinity and, using the smooth behavior of the summand for large m, approximated the correction term by an integration. For $J^0(m)=-J/|m|^3$, this correction term leads to contributions in $H^0_{k,k}$ and $H^0_{k,k'}$ starting at the order $1/N_1^2\sim\phi^2$, which is the highest order in ϕ that we will be interested in keeping. The error made in transforming the summation in this correction term into an integration appears

only in terms on the order of ϕ^3 and higher, which will be neglected. Using various standard summations for combinations of trigonometric functions and powers[26] and the approach developed in Ref. 22 to evaluate $\Sigma_{m=1}^{\infty}\cos(k\phi m)/m^3$ for ϕ small, for $k \ll N_1$ and neglecting terms of order ϕ^3 and higher, we arrive at

$$H^0_{k,k} = \omega_0 - 2J\zeta(3) + J\phi^2[k^2(3/2 - \ln(k\phi)) - f(k)]. \tag{10}$$

Here, $\zeta(x)$ is the Riemann zeta function, with $\zeta(3) = 1.202\ldots$, and $f(k)$ is defined as

$$f(k) = k/2 - k^2\,\mathrm{ci}(\pi k) + (k/\pi)\,\mathrm{si}(\pi k), \tag{11}$$

with $\mathrm{si}(x)$ and $\mathrm{ci}(x)$ the sine and cosine integral functions, respectively.[26] The term $f(k)$ in Eq. (10) gives a correction to the dispersion relation derived in Ref. 22, which results from the correction integral in Eq. (9).

In a similar way, the nondiagonal matrix elements ($k \neq k'$) we arrive at

$$H^0_{k,k'} = -\frac{1+(-1)^{k-k'}}{2}\,a(k,k')J\phi^2, \tag{12}$$

with

$$a(k,k') = \frac{kk'}{k+k'} - \frac{2}{\pi}\,\frac{kk'^2\,\mathrm{si}(\pi k') - k'k^2\,\mathrm{si}(\pi k)}{k^2 - k'^2}. \tag{13}$$

As above, we neglected terms of order ϕ^3 and higher. The second term in Eq. (13) is due to the correction integral in Eq. (9).

From Eqs. (6), (10), and (12), we arrive at

$$r_0(k,k') = \frac{1+(-1)^{k+k'}}{2}\left|\frac{a}{b\,\ln(N_1+1)+c}\right|, \tag{14}$$

where a stands for $a(k,k')$ defined above, $b = k'^2 - k^2$, and $c = f(k) - f(k') + k^2\ln(\pi k e^{-3/2}) - k'^2\ln(\pi k' e^{-3/2})$. It is now clear that $r_0(k,k')$ goes to zero logarithmically for N_1 large, implying that for long chains (cylinders), the ansatz Eq. (5) is a good approximation to the exact eigenstates for k on the order of unity. If we consider the superradiant state $k=1$, its strongest mixing occurs with the state $k'=3$. Substituting these values in the above expressions, gives $a = 1.50734$, $b = 8$, and $c = -9.03323$. For $N_1 = 50$, 100, and 250, this gives $r_0(1,3) = 0.067$, 0.054, and 0.043, respectively, which clearly indicates the smallness of the mixing between these two states.

We note that in Ref. 22 the validity of the ansatz Eq. (5) for the case of point–dipole interactions was argued by directly calculating the ratio of $H_{k,k'}$ ($k \neq k'$) with the energy $H_{k,k}$ and not with the energy difference, as we did. This ratio was found to be of the order $1/(N_1+1)$. We believe the right criterion involves the energy difference, which still shows that the validity of the ansatz improves with growing system length N_1, but only logarithmically.

We end this section by discussing the effects of the deviation of the actual interaction $J^0(m)$ from the point–dipole form considered above. In Appendix B, we show that for cylinders that have a large aspect ratio $N_1 h/2R$, the logarithmic N_1 dependence Eq. (14) still holds, albeit with possibly different coefficients a, b, and c. In the special case that $h > 2R$, $J^0(m)$ for all m may be expressed through a convergent multipole expansion (Appendix A), and only the coefficient c changes to a new value, given by Eq. (B5). If $h < 2R$, the coefficients a and b also obtain new values. In general, the values of the coefficients a, b, and c depend on the structural parameters of the cylinder ($h/2R$, N_2, α, β, and γ). In Sec. V, we will numerically address these values when discussing the example of chlorosomes of green bacteria.

IV. EIGENSTATES OF H^1

We now turn to H^1, which in contrast to H^0 is complex and asymmetric. Again, we base our ansatz for finding the optically dominant wave functions on the solution for a chain with nearest-neighbor interactions, which now are complex. This yields

$$|k\rangle = \sqrt{\frac{2}{N_1+1}}\sum_{n=1}^{N_1}\sin(k\phi n)e^{in(\theta+\gamma)}|n\rangle, \tag{15}$$

with $\phi = \pi/(N_1+1)$ and $k = 1,2,\ldots,N_1$, as before. In the notation of Ref. 18 the state Eq. (15) takes the form of Eq. (47) in that reference, with k replacing k_1 and $\theta+\gamma$ replacing $\theta_{k_2=1}$. The latter represents a phase angle which, in the case where only a nearest-neighbor interaction occurs, is given by the phase of this interaction, $\arg[J^1(1)]$. We have chosen to separate the role of the helical angle γ in this phase angle, as this simplifies the expressions below. Moreover, as we will see in Sec. V, θ is the part of the phase angle that leads to chiral behavior of the wave function on the cylinder surface. As we are dealing with effective long-range interactions, instead of nearest-neighbor ones, it is not clear *a priori* on what interaction to base the total phase angle. Therefore, we will consider θ a free parameter, which will be fixed in order to optimize the quality of the ansatz Eq. (15) for the optically dominant states in the band.

Following the same steps as we did for the $k_2 = 0$ band, we first look where in the $k_2 = 1$ band the optically dominant states occur. The oscillator strength $M(k)$ of states of the type Eq. (15) was already derived as Eq. (50) in Ref. 18. Normalizing the result to the total oscillator strength $N_1 N_2 \mu^2$, the result reads

$$M(k) = \frac{1}{2N_1(N_1+1)}\left[\frac{\sin[N_1(k\phi-\theta)/2]}{\sin[(k\phi-\theta)/2]} - (-1)^k\frac{\sin[N_1(k\phi+\theta)/2]}{\sin[(k\phi+\theta)/2]}\right]^2. \tag{16}$$

Analyzing this result we find that for $N_1 \gg 1, |\cot(\theta)|$ three superradiant states occur that are located a finite energy separation above the bottom of the $k_2 = 1$ band. In other words, the superradiant states in the $k_2 = 1$ band do not occur at the lower band edge. These three states are characterized by the wave numbers $k = k^* - 1$, k^*, and $k^* + 1$. Here $k^* = \mathrm{nint}[|\theta|(N_1+1)/\pi]$ with nint the nearest integer function: $|\theta|(N_1+1)/\pi = \mathrm{nint}[|\theta|(N_1+1)/\pi] + \xi$, with $-0.5 < \xi \leq 0.5$ the remainder.

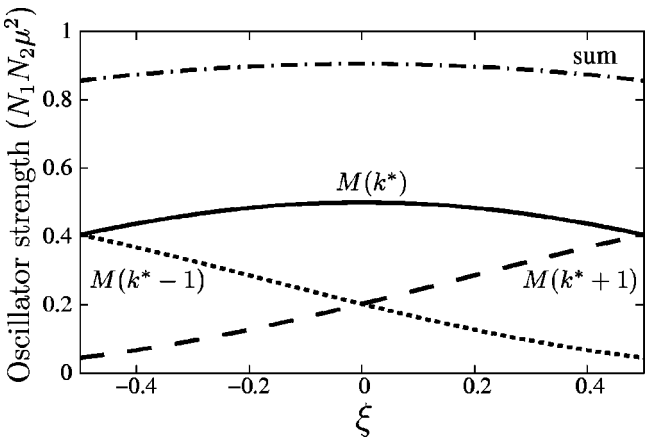

FIG. 2. Oscillator strengths (in units of $N_1N_2\mu^2$) of the three states $k=k^*-1$, k^*, and k^*+1 in the $k_2=1$ band as a function of the mismatch ξ between k^* and $|\theta|(N_1+1)/\pi$ in the limit of $N_1\gg 1$, $|\cot\theta|$ [cf. Eqs. (17) and (18)]. The dot-dashed line gives the total oscillator strength in these three transitions.

If $N_1\gg 1,|\cot(\theta)|$, the oscillator strength of the three superadiant states is to a good approximation given by

$$M(k^*)=\frac{1}{2}\left[\frac{\sin\pi\xi/2}{\pi\xi/2}\right]^2, \tag{17}$$

and

$$M(k^*\pm 1)=\frac{1}{2}\left[\frac{\sin\pi(\xi\mp 1)/2}{\pi(\xi\mp 1)/2}\right]^2. \tag{18}$$

These results are plotted as functions of ξ in Fig. 2. We see that k^* carries roughly half of the total oscillator strength, while the states $k^*\pm 1$ are complementary and together carry roughly the other half. The three states together carry between 85.6% and 90.5% of the total strength in the $k_2=1$ band (in the limit of large N_1).

In direct analogy with the H^0 case, the smallness of the mixing ratio $r_1(k,k')=|H^1_{k,k'}|/(|H^1_{k,k}-H^1_{k',k'}|)$, with $H^1_{k,k'}=\langle k|H^1|k'\rangle$, seems a good criterion for the validity of the ansatz Eq. (15). Since we now deal with three superradiant states, we should consider the various ratios involving these states. However, as two of these states $(k^*\pm 1)$ have complementary behavior of the oscillator strength as a function of N_1, it is more appropriate to weigh the mixing ratio by the corresponding oscillator strengths. We will therefore consider as criterion for the validity of the ansatz Eq. (15) for the optically dominant states the smallness of the weighted mixing ratio

$$\tilde{r}_1(k,k')=(M(k)+M(k'))\frac{|H^1_{k,k'}|}{|H^1_{k,k}-H^1_{k',k'}|}, \tag{19}$$

with $k=k^*-1$, k^*, or k^*+1 and k' one of the neighboring states of k.

The diagonal matrix elements of the Hamiltonian H^1 read

$$H^1_{k,k}=\omega_0+J^1(0)+2\sum_{m=1}^{N_1-1}J^1_+(m)\cos(k\phi m)+\frac{2}{N_1+1}\left[\cot(k\phi)\sum_{m=1}^{N_1-1}J^1_+(m)\sin(k\phi m)-\sum_{m=1}^{N_1-1}mJ^1_+(m)\cos(k\phi m)\right], \tag{20}$$

with

$$J^1_\pm(m)=\tfrac{1}{2}[J^1(m)e^{-im(\theta+\gamma)}\pm\text{c.c.}]. \tag{21}$$

Clearly, $J^1_+(m)$ is real and, owing to the fact that H^1 is Hermitian, we also have $J^1_+(-m)=J^1_+(m)$; conversely, $J^1_-(m)$ is imaginary and $J^1_-(-m)=-J^1_-(m)$. We note that the diagonal element Eq. (20) is identical in form to Eq. (7), with $J^1_+(m)$ replacing $J^0(m)$. Naturally, the diagonal matrix elements are real. By contrast, the off-diagonal elements $H^1_{k,k'}$ $(k\neq k')$ are complex and we will split them into their real and imaginary parts. As we will see, these parts behave fundamentally different for small ϕ.

The real part of $H^1_{k,k'}$ is nonzero only if $k-k'$ is even and reads

$$\text{Re}\,H^1_{k,k'}=\frac{1+(-1)^{k-k'}}{2(N_1+1)}\left\{\cot\frac{(k+k')\phi}{2}\sum_{m=1}^{N_1-1}J^1_+(m)\times[\sin(k\phi m)+\sin(k'\phi m)]-\cot\frac{(k-k')\phi}{2}\times\sum_{m=1}^{N_1-1}J^1_+(m)[\sin(k\phi m)-\sin(k'\phi m)]\right\}, \tag{22}$$

which is identical to $H^0_{k,k'}$ of Eq. (8), except that $J^1_+(m)$ replaces $J^0(m)$. The imaginary part of the off-diagonal matrix elements appears as a new ingredient in the $k_2=1$ Hamiltonian; it is only nonzero if $k-k'$ is odd and reads

$$\text{Im}\,H^1_{k,k'}=\frac{1-(-1)^{k-k'}}{2i(N_1+1)}\left\{\cot\frac{(k+k')\phi}{2}\sum_{m=1}^{N_1-1}J^1_-(m)\times[\sin(k\phi m)-\sin(k'\phi m)]-\cot\frac{(k-k')\phi}{2}\times\sum_{m=1}^{N_1-1}J^1_-(m)[\sin(k\phi m)+\sin(k'\phi m)]\right\}. \tag{23}$$

Before estimating the various summations involved in the above expressions, it is useful to notice that, as we show in Appendix C, we may exclude the case $\theta=0$ (nonchiral wave functions) in order to obtain a good approximation to the wave function. The reason is that $\theta=0$ yields a (weighted) mixing ratio that diverges for large N_1. As argued below Eq. (16), for $\theta\neq 0$, the three superradiant states k^*, $k^*\pm 1$ do not occur at the bottom of the $k_2=1$ band (except if N_1 is very small, which is not of our interest).

Rather the region of interest is characterized by $k^* = \mathrm{nint}[|\theta|/\phi] = \mathrm{nint}[|\theta|(N_1+1)/\pi]$. Hence, unlike the situation in the $k_2=0$ band, the k values of the superradiant states in the $k_2=1$ band are not fixed, but scale linearly with N_1. This scaling complicates the treatment of $H^1_{k,k}$, $\mathrm{Re}\,H^1_{k,k'}$, and $\mathrm{Im}\,H^1_{k,k'}$ in a way directly analogous to Sec. III, as the quantity $k\phi$, which could be considered of the order ϕ in the previous section, now becomes essentially a constant in ϕ. We thus have to be more careful in dealing with the orders of ϕ. As we will be primarily interested in states with k values close to k^*, we may consider $\tilde{r}(k,k')$ with $k=k^*+p$ and $k'=k^*+q$, where p and q are integers of the order of unity and $p\neq q$. Since $k^*\phi = |\theta| - \xi\phi$ with $-0.5 < \xi \leqslant 0.5$, we have $k\phi = |\theta| + (p-\xi)\phi$ and $k'\phi = |\theta| + (q-\xi)\phi$. For N_1 large, $(p-\xi)\phi$ and $(q-\xi)\phi$ are small, on the order of ϕ, and may be used as an expansion parameter in the various functions that occur in the matrix elements Eqs. (20), (22), and (23).

The results of this procedure are as follows. For the energy difference, neglecting terms of the order ϕ^2 and higher, we find

$$H^1_{k^*+p,k^*+p} - H^1_{k^*+q,k^*+q} = -2(p-q)S(\theta)\phi, \tag{24}$$

with $S(\theta) = \Sigma_{m=1}^{N_1-1} J^1_+(m)\, m \sin(m|\theta|)$. Similarly, the real parts of the coupling elements read (up to order ϕ)

$$\mathrm{Re}\,H^1_{k^*+p,k^*+q} = -\frac{1+(-1)^{p-q}}{\pi} S_r(\theta)\phi, \tag{25}$$

with $S_r(\theta) = \Sigma_{m=1}^{N_1-1} J^1_+(m)[m\cos(m\theta) - \cot(\theta)\sin(m\theta)]$. Clearly, the functions $S(\theta)$ and $S_r(\theta)$ only depend on ϕ (or N_1) through the upper summation boundary and a possible dependence of θ on N_1. Both dependencies are weak (see below for the N_1 dependence of θ) and do not add systematic orders of ϕ to the matrix elements. Hence, both $H^1_{k^*+p,k^*+p} - H^1_{k^*+q,k^*+q}$ and $\mathrm{Re}\,H^1_{k^*+p,k^*+q}$ have as leading contributions terms that are linear in ϕ.

The imaginary part of $H^1_{k^*+p,k^*+q}$ requires more care. Substituting the above expressions for $k\phi = (k^*+p)\phi$ and $k'\phi = (k^*+q)\phi$ into Eq. (23), applying several standard manipulations of trigonometric functions, and expanding in powers of ϕ yields (neglecting terms of the order ϕ^2 and higher)

$$\mathrm{Im}\,H^1_{k^*+p,k^*+q} = -\frac{1-(-1)^{p-q}}{\pi \mathrm{i}}\left[\frac{2}{p-q} S_{i1}(\theta) + \frac{p+q-2\xi}{p-q} S_{i2}(\theta)\phi\right], \tag{26}$$

with $S_{i1}(\theta) = \Sigma_{m=1}^{N_1-1} J^1_-(m)\sin(m|\theta|)$ and $S_{i2}(\theta) = \Sigma_{m=1}^{N_1-1} J^1_-(m)\cos(m|\theta|)$. We thus find that, unless $S_{i1}(\theta)$ vanishes, the mixing ratio $\tilde{r}_1(k^*+p,k^*+q)$ has a leading contribution proportional to $1/\phi$, which grows for increasing N_1. The conclusion would be that the ansatz Eq. (15) is not very useful and, contrary to our expectations, deteriorates for growing N_1. We can avoid this situation by demanding that the angle θ is such that $S_{i1}(\theta)$ vanishes, i.e., we fix the choice of $\theta = \theta_0$ such that

$$\sum_{m=1}^{N_1-1} J^1_-(m)\sin(m|\theta_0|) = 0. \tag{27}$$

Notice that, as argued earlier, we do not admit the trivial solution $\theta_0 = 0$ of this condition.

After having set $\theta = \theta_0$, the $S_{i2}(\theta_0)$ term in Eq. (26) gives the leading contribution (order ϕ) in $\mathrm{Im}\,H^1_{k^*+p,k^*+q}$. Combining this with Eqs. (24) and (25) shows that the leading contribution to $\tilde{r}_1(k^*+p,k^*+q)$ is of order unity and reads

$$\tilde{r}_1(k^*+p,k^*+q) = \begin{cases} \dfrac{[M(k^*+p)+M(k^*+q)]}{\pi|p-q|}\dfrac{|S_r(\theta_0)|}{|S(\theta_0)|}, & p-q \ \text{ even} \\ \dfrac{[M(k^*+p)+M(k^*+q)]|p+q-2\xi|}{\pi(p-q)^2}\dfrac{|S_{i2}(\theta_0)|}{|S(\theta_0)|}, & p-q \ \text{ odd.} \end{cases} \tag{28}$$

The important difference with the ratio r_0 in the $k_2=0$ band is that $\tilde{r}_1$ does not systematically decrease with increasing N_1. Hence, the quality of the ansatz Eq. (15) does not improve with growing cylinder size. The solutions for θ_0 and the numerical value of the ratio $\tilde{r}_1$ close to the superradiant transitions will be studied for the special case of chlorosomes in Sec. V.

V. APPLICATION TO CHLOROSOMES AND DISCUSSION

We now consider as an example of cylindrical aggregates the rod elements of chlorosomal antennae of green bacteria[2,3,5,6] and apply the above formalism to calculate the opticaly dominant states and resulting spectra. The parameters for the BChl *c* aggregates of *Chloroflexus aurantiacus* are: $R = 2.297$ nm, $N_2 = 6$, $h = 0.216$ nm, $\alpha = 189.6°$, $\beta = 36.7°$, and $\gamma = 20°$.[27] The length N_1 of these aggregates may extend to hundreds of rings. Furthermore, we have taken ω_0 to agree with a single-molecule absorption peak at 675 nm and, in order to calculate the intermolecular interactions [Eq. (A1)], we have used $\mu^2 = 20\ \mathrm{De}^2$ for the square of the single-molecule transition dipole.

We first consider the validity of the ansatz Eq. (5) for the

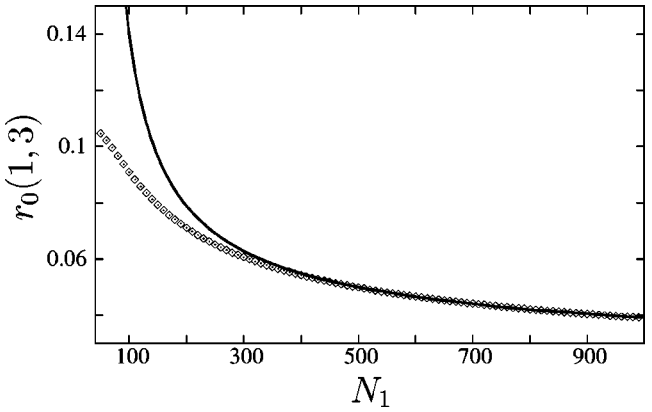

FIG. 3. The ratio $r_0(1,3)$ as a function of N_1 for cylindrical aggregates of the chlorosome structure. The diamonds are the exact values obtained by numerically evaluating $H^0_{1,3}/|H^0_{1,1}-H^0_{3,3}|$, while the solid line represents a fit of the large N_1 behavior to the limiting analytical expression Eq. (14), using b/a and c/a as free parameters.

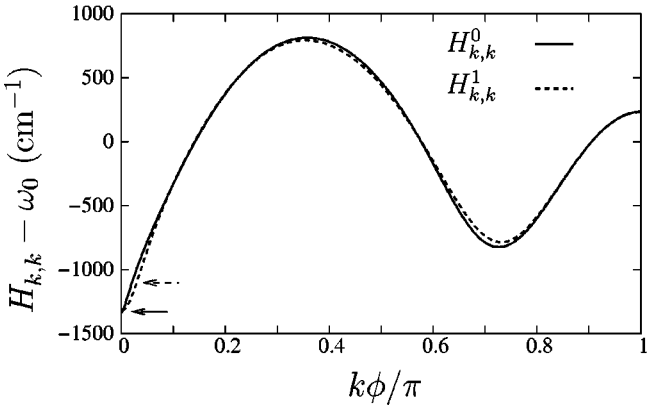

FIG. 5. Unperturbed dispersion relations $H^0_{k,k}$ (solid) and $H^1_{k,k}$ (dashed) as a function of $k\phi$ for $N_1\to\infty$. Structural parameters used are those that apply to the chlorosomes of green bacteria. The solid and dashed arrows indicate the energies of the superradiant states in the $k_2=0$ and the $k_2=1$ bands, respectively.

$k_2=0$ band. In Fig. 3, we plotted as diamonds the exact ratio $r_0(1,3)$ as a function of the cylinder length N_1, numerically calculated from Eqs. (6), (7), and (8) [the ratio $r_0(1,2)$ vanishes identically]. Clearly, the ratio $r_0(1,3)$ already is small for intermediate length ($N_1\approx 100$) and reduces even further when increasing N_1. The solid line in Fig. 3 shows a fit of the exact data in the interval $700\leqslant N_1\leqslant 1000$ to the expression Eq. (14), using b/a and c/a as fit parameters. Although, due to the deviation of the effective interactions $J^0(m)$ from point-dipole ones at small m values, the best-fit parameters ($b/a=8.00$ and $c/a=-29.75$) differ from the ones obtained analytically in Sec. III, the large N_1 dependence clearly follows the logarithmic behavior generally predicted in that section. The obtained values for $r_0(1,3)$ suggest that Eq. (5) is already a good approximation for the optically dominant state in the $k_2=0$ band for cylinders of intermediate length (chlorosomes as short as 20 nm) and that the approximation further improves for increasing N_1. This is demonstrated directly in Fig. 4, where the (n_1 dependence of the) ansatz wave function for $k=1$ is compared to the optically dominant wave function as obtained from numerical diagonalization of H^0 for several values of N_1. Finally, we have plotted in Fig. 5 (solid line) the numerically obtained unperturbed dispersion relation $H^0_{k,k}$ in the $k_2=0$ band for $N_1\to\infty$. This plot clearly demonstrates that, as assumed in Sec. III, indeed $H^0_{k,k}$ does not exhibit degeneracies between the superradiant $k=1$ bottom state (solid arrow) and the higher-lying k states.

We now turn to the $k_2=1$ band and the ansatz Eq. (15). At convergence ($N_1\to\infty$), numerically solving the condition Eq. (27) yields the chiral angle $\theta_0=4.3035°$. Although this angle is small, we will see that it plays a crucial role in the optical properties, in particular in the CD spectrum. As is demonstrated in Fig. 6, the N_1 dependence of θ_0 is weak, a fact that was anticipated below Eq. (25) already. The value of θ_0 at large N_1 implies that the three superradiant states in the $k_2=1$ band are located around $k^*\approx|\theta|(N_1+1)/\pi\approx 0.0239(N_1+1)$. The dashed curve in Fig. 5 gives the numerically obtained unperturbed dispersion relation $H^1_{k,k}$ in the $k_2=1$ band for $N_1\to\infty$ (using $\theta_0=4.3035°$). The dashed arrow in this plot indicates the energy of the three superradiant states (at $k\phi/\pi\approx 0.0239$), which again demonstrates that no degeneracies exist between the superradiant states and the higher-lying k states, implying that we may indeed solely concentrate on the weighted ratios $\tilde{r}_1(k,k')$ for k and

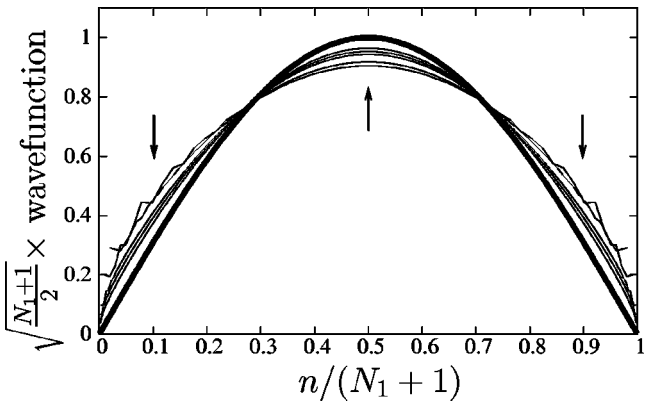

FIG. 4. Comparison between the ansatz wave function Eq. (5) with $k=1$ in the $k_2=0$ band (thick solid line) to the superradiant state in this band found by numerical diagonalization of H^0 for various cylinder lengths (thinner lines). Structural parameters used are those that apply to the chlorosomes of green bacteria. The numerical solutions correspond, in the direction of the arrows, to $N_1=50$, 100, 300, 500, and 1000, respectively.

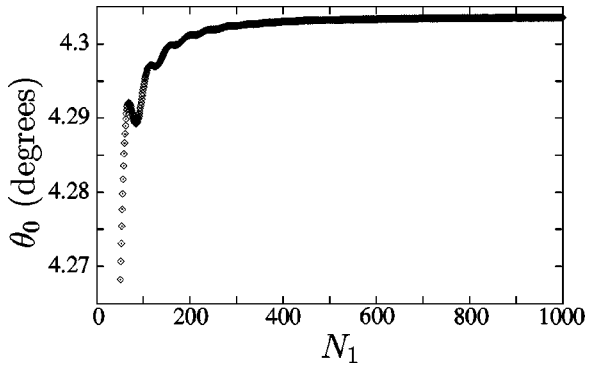

FIG. 6. The chiral angle θ_0, obtained by numerically solving Eq. (27), as a function of the cylinder length N_1. Structural parameters used are those that apply to the chlorosomes of green bacteria.

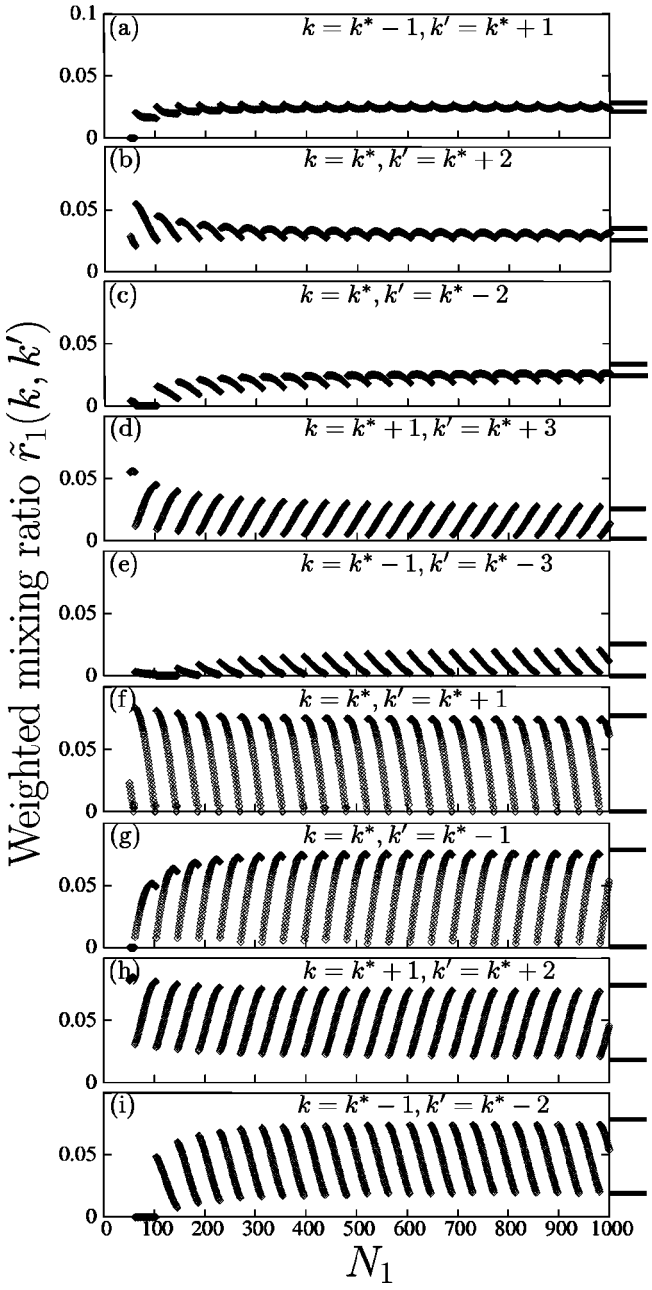

FIG. 7. The weighted mixing ratio $\tilde{r}_1(k,k')$ for nine pairs of states k and k' close around the superradiant transitions in the $k_2=1$ band for cylindrical molecular aggregates of the chlorosome structure. The lines on the left axis indicate the upper and lower boundaries in the large N_1 limit given in Table I.

k' in the immediate vicinity of k^*. This yields in total nine ratios of interest to be considered, all of which are plotted as a function of N_1 in Fig. 7, as obtained from numerically evaluating the matrix elements Eqs. (20), (22), and (23). Panels (a)–(e) involve combinations of states in which the real coupling $\mathrm{Re}\,H^1_{k,k'}$ is nonzero, while the imaginary coupling $\mathrm{Im}\,H^1_{k,k'}$ vanishes and vice versa for panels (f)–(i).

Several comments are in place concerning these results. First, we observe that the ratios oscillate as a function of N_1, which is a consequence of the fact that the remainder ξ defined above Eq. (17) oscillates. This remainder enters $\tilde{r}_1(k,k')$ because the expression for k^* in terms of θ contains

TABLE I. Lower and upper boundaries for the weighted mixing ratio $\tilde{r}_1(k,k')$ in the limit of long cylinders for various combinations of k and k' close to the superradiant transitions in the $k_2=1$ band. Structural parameters used are those for the chlorosomes of green bacteria. The values in the table were derived using Eq. (28).

k	k'	$\tilde{r}^{\infty}_{1,\min}$	$\tilde{r}^{\infty}_{1,\max}$
k^*-1	k^*+1	0.0236	0.0263
k^*	$k^*\pm 2$	0.0246	0.0292
$k^*\pm 1$	$k^*\pm 3$	0.0031	0.0246
k^*	$k^*\pm 1$	0	0.0736
$k^*\pm 1$	$k^*\pm 2$	0.0200	0.0736

ξ. Second, we see that the weighted ratios are small over the entire range of N_1 values considered ($N_1>50$), suggesting that the ansatz Eq. (15) is a good approximation for the optically dominant wave functions. Third, we see that in contrast to the ratio r_0 in the $k_2=0$ band, $\tilde{r}_1(k,k')$ does not tend to zero in the limit of large N_1. This agrees with the small ϕ expansion made in Sec. IV [Eq. (28)], which indicated that the leading contribution to $\tilde{r}_1(k,k')$ is zeroth order in ϕ. In the limit of large N_1, the weighted ratio $\tilde{r}_1(k,k')$ oscillates between two boundaries, which may be calculated analytically using the $N_1\to\infty$ values of the summations $S(\theta_0) = -1881\ \mathrm{cm}^{-1}$, $S_r(\theta_0)=691\ \mathrm{cm}^{-1}$, and $S_{i2}(\theta_0) = 483\ \mathrm{cm}^{-1}$. The resulting boundaries for the ratios of interest are given in Table I and agree well with the limiting values observed in Fig. 7.

To further demonstrate the validity of the ansatz Eq. (15) and to clarify the (chiral) nature of the wave functions, in Fig. 8 we plotted the squared amplitude of the wave functions for the three superradiant states $k=k^*-1$, k^*, and k^*+1 as a function of the position on the cylinder surface. To this end, the cylinder was cut along a line parallel to the cylinder's axis (taken as vertical axis in the plots) and unwrapped. To the right of each result obtained from the ansatz is plotted the corresponding exact result obtained by numerically diagonalizing the Hamiltonian H^1. Here, the correspondence was defined through the number of nodes in the wave function along the axis direction. In the example considered here, we used a cylinder with $N_1=300$ rings. For this length we have $k^*=7$, which clearly is reflected in the number of nodes in the wave function along the axis direction. We also see that the ansatz gives an excellent description of the exact wave functions, in particular it describes the slanting of the equal-phase lines away from the vertical in an excellent way. This slanting is a direct consequence of the fact that θ_0 does not vanish (the slant angle is given by θ_0) and is a manifestation of the chiral behavior of the wave function on the cylinder surface. This may easily be seen by considering the complex factor in the amplitude of the total wave function, which reads $\exp[i(\gamma+\theta_0)m_1+i2\pi m_2/N_2]$. We note that going up three rings along the cylinder's surface ($\Delta m_1=3$) and going back one step along the ring ($\Delta m_2=-1$), due to the fact that $N_2=6$ and $\gamma=20°$, is exactly a vertical displacement over the surface, i.e., parallel to the cylinder axis. Clearly, this displacement induces a change $\exp(i\theta_0\Delta m_1)$ in the phase factor, which vanishes for $\theta_0=0$. Hence, the slant angle of equal-phase lines away from the axis direction in-

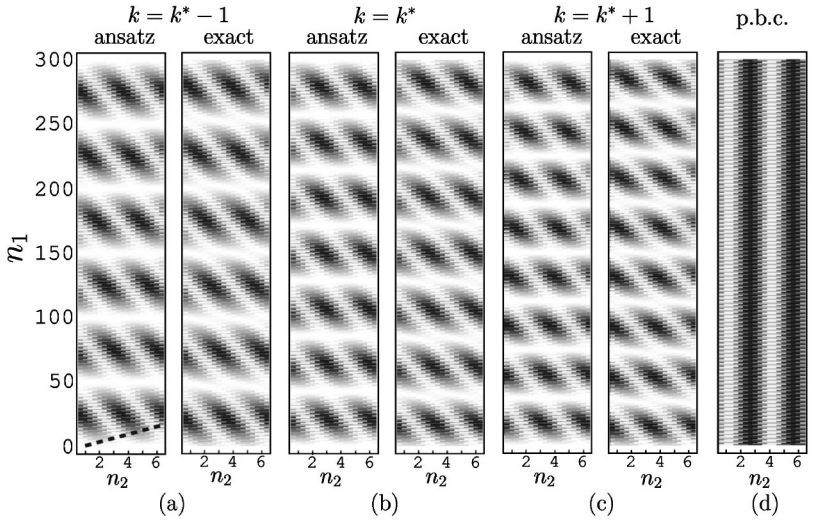

FIG. 8. (a)–(c) Gray-scale plots of the squared amplitudes (darker is larger amplitude) of the three superradiant states in the $k_2=1$ band for cylinders of the chlorosome structure with a length of $N_1=300$ rings. To generate these plots, the cylinder surface is cut along a line parallel to the axis and unrolled. Thus, horizontal lines in the plot correspond to molecules lying on the same ring of the cylinder, having the same position index n_1. Due to the helical structure of chlorosomes, lines of constant n_2 make a finite angle with the vertical direction [the dashed line in panel (a) corresponds to $n_2=1$; also cf. dashed line in Fig. 1]. For each superradiant state, the dependence of the wave function on n_1 given by the ansatz Eq. (15) [with $\theta=\theta_0$ obeying Eq. (27)] is plotted to the left, while for comparison immediately next to the right of it is plotted the corresponding wave function found by numerical diagonalization of H^1. For all plots, the dependence on n_2 is given by the Bloch wave $\exp[i2\pi n_2/N_2]$. For further comparison, we plotted in panel (d) the wave function of the only superradiant state [$\sim\exp(i\gamma n_1+i2\pi n_2/N_2)$] that occurs in the $k_2=1$ band if we impose PBC in the n_1 direction. We note that the ansatz and exact wave functions in (a)–(c) all exhibit a clear chiral behavior, reflected in the slanting of the equal-phase lines with respect to the vertical axis; the slant angle is given by θ_0. Such a chiral behavior is missing in (d).

deed is given by θ_0.[28] We note that if we assume PBC in the n_1 direction, θ_0 vanishes identically for the superradiant state,[18] and the wave functions are nonchiral, having equal-phase lines that coincide with the axis direction. This is demonstrated in Fig. 8, by plotting in panel (d) the squared amplitudes for the only superradiant state that occurs with PBC.

Finally, we demonstrate the power of the two ansätze, Eqs. (5) and (15), for the optically dominant states by calculating the spectra generated from them using the general expressions in Ref. 18. For the energies of the k states in the two bands, we used the values $H^0_{k,k}$ and $H^1_{k,k}$. The thus generated absorpion and CD spectra are given by the solid lines in Fig. 9, for cylinders of $N_1=100$, $N_1=300$, and $N_1=500$ rings long. The dashed and dotted lines give the same spectra generated using exact diagonalization and PBC, respectively. The PBC spectra were calculated in the infinite N_1 limit. The

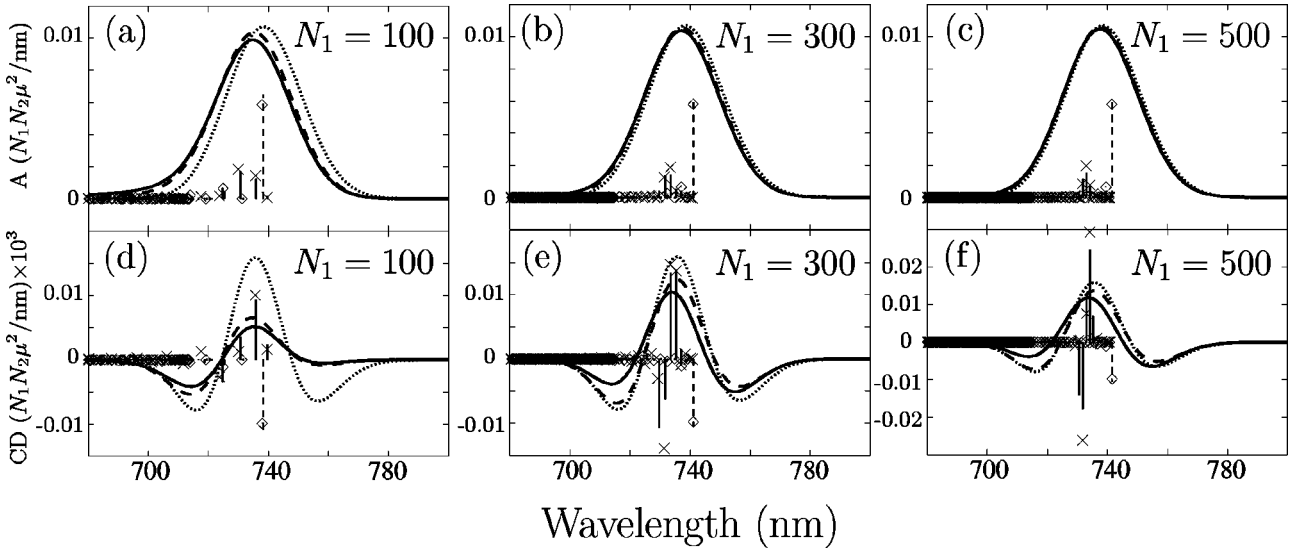

FIG. 9. Absorption spectra [(a)–(c)] and circular dichroism spectra [(d)–(f)] for cylinders of the chlorosome structure with three different lengths N_1. The smooth curves represent the results as obtained from our ansatz wave functions Eqs. (5) and (15) (solid), from exact numerical diagonalization (dashed), and from PBC (dotted). The underlying stick spectra of the numerical solution are also given, with the dashed sticks referring to states in the $k_2=0$ band and the solid ones resulting from the $k_2=\pm1$ bands. The strengths of the transitions obtained from the ansatz wave functions are given as diamonds for the $k_2=0$ band and crosses for the $k_2=\pm1$ bands.

smooth spectra were obtained by convoluting the stick spectra at the exciton resonances with a Gaussian line shape function of full width at half maximum of 500 cm^{-1}. The stick spectra for the exact diagonalization are presented as dashed lines for the $k_2=0$ band and solid lines for the $k_2=\pm 1$ bands. The strengths of the stick spectra obtained via the analytical ansätze are represented as diamonds for the $k_2=0$ band and crosses for the $k_2=\pm 1$ bands.

From Figs. 9(a)–9(c) it is clear that at all cylinder lengths considered, the absorption spectrum generated by the ansatz wave functions generally is better than the one generated by using PBC. In particular at intermediate lengths, on the order of $N_1=100$, the spectrum has not converged yet to the infinite-length PBC solution, while the analytical ansatz does capture correctly the finite-size effects in the spectral position. Also the comparison between the exact and analytical stick spectra shows how good the comparison is at all lengths. We remind the reader that for the case of PBC, we have only one resonance (one superradiant state) in the $k_2=\pm 1$ bands, while we clearly see that in the finite-size spectra more such states occur.

If we consider Fig. 9(d), we observe that for the CD spectra not only the position, but rather the entire spectral shape, is at intermediate length much better represented by the analytical ansätze for the wave functions than when using PBC. As we discussed in detail in Ref. 18, the CD spectrum converges only very slowly to the PBC result, due to the fact that this spectrum results from subtle interference between close lying positive and negative contributions. This makes the spectrum extremely sensitive to the exact positions of resonances and values of transition dipoles. In fact, as was noted in Sec. I, the poor behavior of the PBC results for the CD spectrum was one of the main motivations to search for better analytical solutions to the wave functions. We observe from the stick spectra that the CD is characterized by more than three strong transitions in the $k_2=\pm 1$ bands. Extra transitions occur in the so-called helical part of the CD spectra,[18] where states $k^*\pm 2$ and further also become important. These states further away from k^* generally turn out not to conform to the ansatz Eq. (15) as well, which is responsible for the fact that for increasing cylinder length the ansatz spectrum does not fully converge to the exact spectrum, while the PBC spectrum does (albeit at very large length). In particular we observe that for $N_1=500$ the ansatz CD spectrum and the PBC one have roughly equal deviations from the exact spectrum [Fig. 9(f)].

VI. CONCLUSIONS

In this paper, we have investigated approximate analytical solutions for the exciton wave functions of general cylindrical molecular aggregates, in particular for the optically dominant wave functions in the exciton bands with transverse wave number $k_2=0$ and $k_2=\pm 1$. We had a special interest in accounting for a finite cylinder length, i.e., in going beyond the analytical solutions that are obtained when imposing PBC along the cylinder's axis direction. We have found that the two ansätze, Eqs. (5) and (15), which are inspired on solutions for cylinders in which only interactions between neighboring rings in the cylinder occur, give good approximations even when we include all long-range dipole–dipole interactions between the molecules in the aggregate.

We have found that a fundamental difference exists between the $k_2=0$ band and the $k_2=\pm 1$ bands. In the former case, the effective one-dimensional Hamiltonian that has to be solved is real and symmetric and we have shown quite generally that the ansatz Eq. (5) for the optically dominant states at the bottom of the band improves logarithmically for increasing cylinder length. For the $k_2=\pm 1$ bands, the Hamiltonian is complex and asymmetric and the ansatz Eq. (15) does not improve systematically with cylinder size. We have shown that the phase angle θ in this ansatz can be determined by requiring the ansatz to be optimal [Eq. (27)] and that the thus obtained angle θ_0 determines the chiral nature of the wave functions as reflected in the slanting of the equal-phase lines when plotting the wave functions on the cylinder surface (Fig. 8). In, case we impose PBC along the cylinder axis, this phase angle vanishes. The phase angle is of particular importance for the shape of the CD spectrum: small changes in this angle cause strong effects in this shape.

To illustrate our general formalism, we have used the ansatz wave functions to describe the exciton states and resulting absorption and CD spectra for the chlorosomes of green bacteria, and compared the results to those obtained

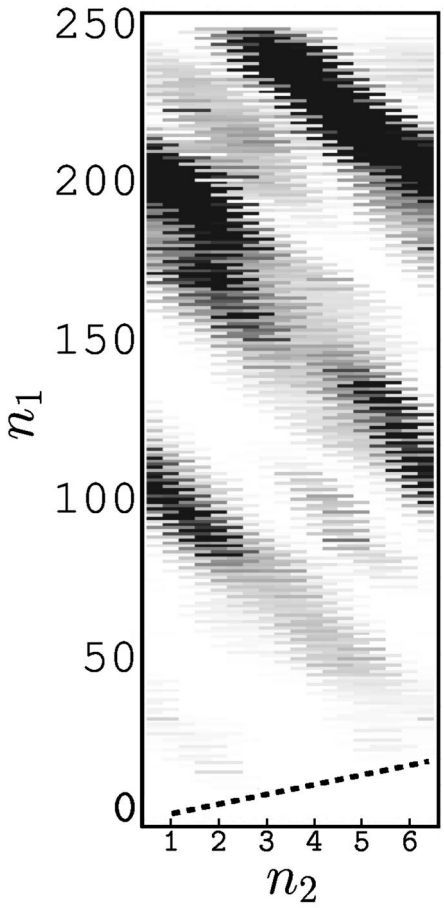

FIG. 10. Amplitude squared on the unrolled cylinder surface (cf. Fig. 8) for a typical wave function obtained numerically when accounting for Gaussian diagonal disorder. Parameters used are those for the chlorosomes of green bacteria of length $N_1=250$ rings, while for the disorder we used a standard deviation of 400 cm^{-1}.

numerically by brute force diagonalization of the Hamiltonian as well as those obtained analytically by using PBC. The results confirm that for cylinder lengths longer than roughly 50 rings, the ansatz wave functions give good descriptions of the optically dominant states and the spectra. This is, in particular for the CD spectrum, far shorter than the length at which the PBC approach gives good results.

As we have demonstrated earlier,[18] in case we impose PBC, three superradiant states dominate the absorption spectrum, one in each of the $k_2=0$ and $k_2=\pm 1$ bands. The ones in the $k_2=\pm 1$ bands are degenerate. In this paper, we found that if we correctly account for finite-length effects, seven superradiant states occur (unless the length is very short): the $k=1$ state in the $k_2=0$ band [Eq. (5)], and the states $k=k^*-1$, k^*, and k^*+1 in the $k_2=\pm 1$ bands [Eq. (15)]. Again, the latter are doubly degenerate. In the limit of long cylinders, the three superradiant states in each of the $K_2=\pm 1$ bands become degenerate, and occur at the same energy as the single superradiant state that exists in these bands if we impose PBC.

We finally notice that we have restricted ourselves in this paper to the homogeneous, cylindrically symmetric, limit (no disorder), which allows us to use the Bloch decomposition in the transverse direction, leading to effective one-dimensional exciton bands. In reality, disorder may play an important role and break the cylindrical symmetry. A study of the effect of disorder will be described elsewhere.[29] In the context of this paper, however, it is of interest to illustrate that even if the disorder is large enough to localize the exciton wave functions, they locally do exhibit the same chiral behavior as the homogeneous solutions. This is clear from Fig. 10, in which we plot the amplitude squared of one of the optically important exciton states found by numerically diagonalizing a random realization of a cylinder with the chlorosome structure and length $N_1=250$ rings, with Gaussian diagonal disorder of standard deviation 400 cm^{-1}. The phase jumps that occur at $n_1\approx 150$ and $n_1\approx 180$ clearly demonstrate the disorder-induced mixing of unperturbed eigenstates. We finally note that inclusion of dynamic disorder through, e.g., a stochastic model, is of interest to study transport properties.[30]

ACKNOWLEDGMENTS

This work is part of the research program of the Stichting voor Fundamenteel Onderzoek der Materie (FOM), which is financially supported by the Nederlandse Organisatie voor Wetenschappelijk Onderzoek (NWO).

APPENDIX A: MULTIPOLE EXPANSION

In this Appendix, we derive multipole expansions for the effective interactions $J^0(m)=J(m;k_2=0)$ and $J^1(m)=J(m;k_2=1)$ defined through Eq. (2). We start from the dipole–dipole interaction on the cylinder, which reads

$$J(m_1,m_2)$$
$$=\frac{\mu^2}{(|m_1|h)^3}\cos^3\varphi\Big\{\cos^2\beta+\sin^2\beta\cos(\phi_2 m_2+\gamma m_1)$$
$$-\frac{3}{2}[\sin^2\beta\sin^2\varphi\,(\cos(2\alpha)+\cos(\phi_2 m_2+\gamma m_1))$$
$$+2\cos^2\beta\cos^2\varphi+\sin(2\beta)\sin(2\varphi)\cos\alpha$$
$$\times\cos(\phi_2 m_2/2+\gamma m_1/2)]\Big\}, \tag{A1}$$

with

$$\tan\varphi=\frac{2R\sin(\phi_2 m_2/2+\gamma m_1/2)}{m_1 h}\equiv y \tag{A2}$$

$(-\pi/2<\varphi<\pi/2)$. To make a multipole expansion, we will need the following expansions (for $|y|<1$):

$$\cos^3(\arctan(y))=\sum_{s=0}^{\infty}(-1)^s\frac{y^{2s}(2s+1)!}{(2^s s!)^2}\equiv\sum_{s=0}^{\infty}\kappa(s,y), \tag{A3}$$

$$\cos^5(\arctan(y))=\sum_{s=0}^{\infty}\frac{2s+3}{3}\kappa(s,y), \tag{A4}$$

$$\cos^3(\arctan(y))\sin^2(\arctan(y))=\sum_{s=0}^{\infty}\frac{2s+3}{3}y^2\kappa(s,y), \tag{A5}$$

$$\cos^3(\arctan(y))\sin(2\arctan(y))=\sum_{s=0}^{\infty}2\frac{2s+3}{3}y\kappa(s,y). \tag{A6}$$

Now the original interaction may be written

$$J(m_1,m_2)$$
$$=\frac{\mu^2}{(|m_1|h)^3}\sum_{s=1}^{\infty}\kappa(s,y)$$
$$\times\Big\{-2(s+1)\cos^2\beta+\sin^2\beta\cos(\phi_2 m_2+\gamma m_1)$$
$$-\frac{2s+3}{2}[\sin^2\beta[\cos(2\alpha)+\cos(\phi_2 m_2+\gamma m_1)]y^2$$
$$+2\sin(2\beta)\cos\alpha\cos(\phi_2 m_2/2+\gamma m_1/2)y]\Big\}. \tag{A7}$$

Furthermore, using the definition of y, we find

$$y^{2s}=\left(\frac{2R}{m_1 h}\right)^{2s}\frac{(-1)^s}{2^{2s}}\sum_{p=0}^{2s}\binom{2s}{p}(-1)^p$$
$$\times\exp[i(s-p)(\phi_2 m_2+\gamma m_1)]. \tag{A8}$$

We may now perform the summation over m_2 in Eq. (2) and, omitting the subscript "1," we get for the effective one-dimensional interaction in the $k_2=0$ band the multipole expansion (valid for $|m|h>2R$)

$$J^0(m)=-\frac{1}{|m|^3}\left[J+\sum_{s=1}^{\infty}\frac{j_s}{m^{2s}}\right], \tag{A9}$$

with

$$J=\frac{2N_2\mu^2\cos^2\beta}{h^3} \tag{A10}$$

and

$$j_s=\frac{(-1)^s(2s+1)!!(2s)!}{2^{3s}(s!)^3}\frac{N_2\mu^2}{h^3}\left(\frac{2R}{h}\right)^{2s}\times 2[-(s+1)\cos^2\beta - s\sin^2\beta\sin^2\alpha]. \tag{A11}$$

In a similar way, we may derive the effective interaction $J^1(m)$ in the $k_2=1$ band which, using the decomposition Eq. (21), yields for $|m|h>2R$ the multipole expansion

$$J^1_+(m)=\frac{1}{|m|^3}\sum_{s=0}^{\infty}\left[\frac{g_s}{m^{2s}}\cos(m\theta)+\frac{h_s}{m^{2s+1}}\sin(m\theta)\right], \tag{A12}$$

and

$$J^1_-(m)=-\frac{i}{|m|^3}\sum_{s=0}^{\infty}\left[\frac{g_s}{m^{2s}}\sin(m\theta)-\frac{h_s}{m^{2s+1}}\cos(m\theta)\right], \tag{A13}$$

with

$$g_{s=0}=\frac{N_2\mu^2\sin^2\beta}{2h^3}, \tag{A14}$$

$$g_{s\geqslant 1}=\frac{(-1)^s(2s+1)!!(2s)!}{2^{3s}(s!)^3}\frac{N_2\mu^2}{h^3}\left(\frac{2R}{h}\right)^{2s}\times\left[(2s)\cos^2\beta+\frac{2s+1}{(s+1)(s+2)}\sin^2\beta+2\frac{s^2}{s+1}\sin^2\beta\sin^2\alpha\right], \tag{A15}$$

and

$$h_s=\frac{(-1)^s(2s+1)!!(2s)!}{2^{3s}(s!)^3}\frac{N_2\mu^2}{h^3}\left(\frac{2R}{h}\right)^{2s+1}\times\frac{(2s+1)(2s+3)}{2(s+1)(s+2)}\sin(2\beta)\cos\alpha. \tag{A16}$$

We observe that J^1_+ is even in m, while J^1_- is odd, as was clear from Eq. (21) already.

APPENDIX B: DEVIATIONS FROM POINT–DIPOLE INTERACTIONS

In this, Appendix, we consider how the deviations of the actual interactions $J^0(m)$ from the point–dipole form affect the ratio $r_0(k,k')$ (k and k' both of the order of unity). We start by assuming that the multipole expansion Eq. (A9) holds for all m, which is the case if $h>2R$. Using the expansion in Eqs. (7) and (8) then gives rise to summations of the type

$$\sum_{m=1}^{\infty}\frac{\cos(km\phi)}{m^{2s}}=(-1)^{s-1}\frac{1}{2}\frac{(2\pi)^{2s}}{(2s)!}B_{2s}(k\phi/2\pi), \tag{B1}$$

and

$$\sum_{m=1}^{\infty}\frac{\sin(km\phi)}{m^{2s+1}}=(-1)^{s-1}\frac{1}{2}\frac{(2\pi)^{2s+1}}{(2s+1)!}B_{2s+1}(k\phi/2\pi), \tag{B2}$$

with B_n the Bernoulli polynomial of degree n.[26] These summations for the special case $s=1$ were used in the main text (Sec. III).

An important property of the Bernoulli polynomials is that for $s\neq 1$ $B_{2s}(x)$ does not contain a term linear in x, while $B_{2s+1}(x)$ does not contain terms linear in x^0 and x^2. Using these properties in Eq. (8), one finds that terms in the expansion Eq. (A9) with $s\geqslant 2$ only give corrections to the result Eq. (12) for $H^0_{k,k'}$ that are on the order ϕ^3 and higher. The corrections due to extending the summations in Eq. (8) to infinity are of the order ϕ^4. As before, we will neglect these contributions beyond the order ϕ^2.

We now turn to $H^0_{k,k}$, given by Eq. (7), which involves summations of the type Eqs. (B1) and (B2) in its last two terms, as well as $\Sigma_{m=1}^{\infty}\cos(k\phi m)/m^{2s+1}$ (third term). Following an approach similar to the one used in Ref. 22 for evaluating the latter summation for the special case $s=1$ in the small-ϕ limit and neglecting terms of the order ϕ^4 and higher, we arrive at

$$\sum_{m=1}^{\infty}\frac{\cos(km\phi)}{m^{2s+1}}=\begin{cases}\zeta(3)+\frac{1}{2}[-\frac{3}{2}+\ln(k\phi)](k\phi)^2, & \text{for } s=1\\ \zeta(2s+1)-\frac{1}{2}\zeta(2s-1)(k\phi)^2, & \text{for } s\geqslant 2\end{cases} \tag{B3}$$

with ζ the Riemann zeta function (this summation for $s=1$ was used in Sec. III). We thus find that the higher-order multipole interactions ($s\geqslant 2$) in the third term of Eq. (7) contribute terms of the order ϕ^0 and ϕ^2. Moreover, from Eqs. (B1) and (B2) and the special properties of the Bernoulli polynomials, we find that the higher-order multipole interactions contribute to the last two terms in Eq. (7) together, with only corrections of the order ϕ^3 and higher (terms of the order ϕ cancel). Hence, up to and including terms of the order ϕ^2, the total contribution of the higher-order multipole interactions to $H^0_{k,k}$ is given by adding to Eq. (10) a term $\delta H^0_{k,k}$ defined by

$$\delta H^0_{k,k}=\sum_{s=2}^{\infty}[2j_s\zeta(2s+1)-j_s\zeta(2s-1)k^2\phi^2]. \tag{B4}$$

Combining the thus obtained corrections $H^0(k,k)$ and $H^0(k,k')$ due to the higher-order multipole interactions, we find that, if $h>2R$, the ratio $r_0(k,k')$ still has the form Eq. (14), except that the coefficient c is replaced by

$$c'=c+\sum_{s=2}^{\infty}\frac{j_s}{J}(k^2-k'^2)\zeta(2s-1). \tag{B5}$$

We finally make the step to the situation of more general interest, where $2R$ is not smaller than h and, thus, the multipole expansion can only be applied from a certain value $m_c=\text{int}[2R/h]>1$ for the intersite separations m. As long as the cylinder has an aspect ratio $N_1h/2R\gg 1$ (which is a physically obvious assumption to make for cylindrical aggregates), we have $m_c\ll N_1$. To treat this general situation, we split the summations of interest as follows ($\alpha=0$ or 1):

$$\sum_{m=1}^{N_1-1} m^{\alpha} J^0(m) F(m\phi) = \sum_{m=1}^{m_c} m^{\alpha} J^0(m) F(m\phi) + \sum_{m=m_c+1}^{N_1-1} m^{\alpha} J^0(m) F(m\phi), \tag{B6}$$

where in the second right-hand side term we use the multipole expansion Eq. (A9) for $J^0(m)$, while in the first we cannot. The first summation on the right-hand side can be estimated by using a Taylor expansion for the sines and the cosines described by F, because for k on the order of unity $km\phi$ is a small number over the range $1 \leqslant m \leqslant m_c$. By doing this it can be shown that for $H^0_{k,k} - H^0_{k',k'}$ this first summation contributes terms of the order ϕ^2 and higher, while for $H^0_{k,k'}$ it only contributes terms of the order ϕ^3 and higher. This again implies a correction of the coefficient c in Eq. (14).

We now turn to estimating the contributions generated by the second term in Eq. (B6), where we use the multipole expansion for the interactions $J^0(m)$. Of course, the previous discussion concerning the corrections due to extending the summations to infinity remains valid. Thus, the only remaining question is what is the contribution due to the missing terms $m=1,\ldots,m_c$ in the summations. Again by using Taylor expansions of the functions $F(m\phi)$ in the range $1 \leqslant m \leqslant m_c$ it can be proven that these missing terms in the summations Eqs. (B1), (B2), and (B3) do not change the orders occurring in ϕ, but only the coefficients in the expansions. Hence, the general result for $r_0(k,k')$ is still given by Eq. (14), except that the coefficients a, b, and c obtain different values, which depend on the detailed structure of the cylinder.

APPENDIX C: EXCLUSION OF $\theta=0$

In this Appendix, we argue that $\theta=0$ does not render the ansatz Eq. (15) a good approximation for the optically dominant states. In this special case, we have $\cot\theta \to \infty$, which makes Eqs. (17) and (18) invalid. Instead, we can see directly from Eq. (16) that the only superradiant state now is the one with $k=1$, which for a usual J-aggregate dispersion lies at the bottom of the $k_2=1$ band. Now we can closely follow the treatment of Sec. III. Setting $\theta=0$ in the multipole expansions for J^1_+ and J^1_- given in Eqs. (A12) and (A13), respectively, we find in direct analogy with Sec. III that $H^1_{k,k} - H^1_{k',k'}$ has a leading contribution of the order $\phi^2 \ln\phi$, while $\mathrm{Re}\, H^1_{k,k'}$ has a leading contribution of the order ϕ^2. Moreover, it turns out that $\mathrm{Im}\, H^1_{k,k'}$ in the case $\theta=0$ contains terms of order ϕ, which is a consequence of the fact that, unlike for the cases of $\mathrm{Re}\, H^1_{k,k'}$ and $H^0_{k,k'}$, the terms of order ϕ do not cancel, because $(k-k')/(k+k') - (k+k')/(k-k') \neq 0$. Therefore, we find that if we take $\theta=0$, the (weighted) mixing ratio $\tilde{r}_1$ for the superradiant state (i.e., at the bottom of the band) is of the order $N_1/\ln N_1$, which diverges for growing N_1, making the ansatz useless.

[1] L. A. Staehelin, J. R. Golecki, and G. Drews, Biochim. Biophys. Acta **589**, 30 (1980).
[2] A. R. Holzwarth and K. Schaffner, Photosynth. Res. **41**, 225 (1994).
[3] V. I. Prokhorenko, D. B. Steengaard, and A. R. Holzwarth, Biophys. J. **79**, 2105 (2000).
[4] V. I. Prokhorenko, D. B. Steensgaard, and A. R. Holzwarth, Biophys. J. **85**, 3173 (2003).
[5] T. S. Balaban, A. R. Holzwarth, and K. Schaffner, J. Mol. Struct. **349**, 183 (1995).
[6] B. J. van Rossum, G. J. Boender, F. M. Mulder *et al.*, Spectrochim. Acta, Part A **54**, 1167 (1998).
[7] A. Pawlik, S. Kirstein, U. D. Rossi, and S. Dähne, J. Phys. Chem. B **101**, 5646 (1997).
[8] S. Kirstein, H. von Berlepsch, C. Böttcher, C. Burger, A. Ouart, G. Reck, and S. Dähne, ChemPhysChem **3**, 146 (2000).
[9] S. Dähne and K.-D. Nolte, Chem. Commun. **1972**, 1056.
[10] T. Tani, *Photographic Sensitivity* (Oxford University Press, Oxford, 1995).
[11] C. Spitz, J. Knoester, A. Ouart, and S. Dähne, Chem. Phys. **275**, 271 (2002).
[12] M. Bednarz and J. Knoester, J. Phys. Chem. B **105**, 12913 (2001).
[13] S. S. Lampoura, C. Spitz, S. Dähne, J. Knoester, and K. Duppen, J. Phys. Chem. B **106**, 3103 (2002).
[14] H. von Berlepsch, S. Kirstein, and C. Böttcher, Langmuir **18**, 7699 (2002).
[15] H. von Berlepsch, S. Kirstein, R. Hania, C. Didraga, A. Pugžlys, and C. Böttcher, J. Phys. Chem. B **107**, 14176 (2003).
[16] J. D. Hartgerink, E. R. Zubarev, and S. I. Stupp, Curr. Opin. Solid State Mater. Sci. **5**, 355 (2001).
[17] J. H. K. K. Hirschberg, L. Brunsfeld, A. Ramzi, J. A. J. M. Vekemans, R. P. Sijbesma, and E. W. Meijer, Nature (London) **407**, 167 (2000).
[18] C. Didraga, J. A. Klugkist, and J. Knoester, J. Phys. Chem. B **106**, 11474 (2002).
[19] O. J. G. Somsen, R. van Grondelle, and H. van Amerongen, Biophys. J. **71**, 1934 (1996).
[20] F. C. Spano and Z. G. Soos, J. Chem. Phys. **99**, 9265 (1993).
[21] D. Yaron and R. Silbey, Phys. Rev. B **45**, 11655 (1992).
[22] V. Malyshev and P. Moreno, Phys. Rev. B **51**, 14587 (1995).
[23] This holds for N_2 is even; obvious changes apply if N_2 is odd.
[24] R. M. Hochstrasserand J. D. Whiteman, J. Chem. Phys. **56**, 5945 (1972).
[25] H. Fidder, J. Knoester, and D. A. Wiersma, J. Chem. Phys. **95**, 7880 (1991).
[26] I. S. Gradstein and I. M. Ryzhik, *Table of Integrals, Series, and Products* (Academic, New York, 1980).
[27] These parameters are obtained from Refs. 3 and 4, after translating to our stack-of-rings view of the cylinder, as explained in more detail in Ref. 18.
[28] It is to be noted that θ_0 only gives the slant angle averaged over a number of rings. Locally, the discreteness of the lattice causes small deviations in the equal-phase lines, as is clearly seen in Fig. 8.
[29] C. Didraga and J. Knoester (unpublished).
[30] P. Reineker, C. Warns, C. Supritz, and I. Barvík, J. Lumin. **102–103**, 802 (2003).